An Iterative Learning Approach for Online Flight Path Optimization for Tethered Energy Systems Undergoing Cyclic Spooling Motion

Mitchell Cobb[1], Kira Barton[2], Hosam Fathy[3], and Chris Vermillion[4]

Abstract— **This paper presents an iterative learning based approach for optimizing the crosswind flight path of an energy-harvesting tethered system that executes cyclic spool-in/spool-out motions. Through the combination of a high-tension cross-wind spool-out motion (made possible through a high lift wing) and low-tension spool-in motion, net energy is generated at every cycle. Because the net energy generated by the system is highly sensitive to the crosswind flight patterns used on spool-out, and because the motions of the system are repetitive, we use an iterative learning formulation to optimize the flight patterns in real time. Using a medium-fidelity dynamic model, we demonstrate that an optimization approach based on iterative learning control (ILC) significantly increases the average power generated by such a system.**

I. Introduction

Traditional towered wind and marine hydrokinetic (MHK) system designs suffer from the inability to reach high altitude winds and harness ocean currents in deep waters, respectively. In fact, atmospheric characterizations have shown that wind resources at 600m altitude routinely possess over five times the power density of winds at 100m altitude but are unreachable with towered systems [1]. Furthermore, the portion of the Gulf Stream adjacent to Cape Hatteras, NC possesses more power than the electricity demand of the entire state of North Carolina but also lies in waters that are over 500 meters deep, rendering towered systems impractical [2].

Tethered systems for wind and marine hydrokinetic energy, as depicted conceptually in Fig. 1 (a) and (b), break the above impasse, allowing operating at high altitudes (in the case of wind energy) and deep waters (in the case of hydrokinetic energy). The replacement of towers with tethers and a lifting body (wing, kite, or aerostat) additionally enables the systems to utilize motion within the surrounding fluid to enhance energy capture. In fact, [3] has shown that a high lift/drag wing that is flown in *crosswind* motions can generate significantly more energy than one operating in stationary flight. Energy can be generated through one of two mechanisms:

1) *On-board generation:* Here, a rotor is mounted on the wing itself, and power is transmitted to a base station through a conductive cable.
2) *Cylic "ground"-based generation:* In this scenario, the wing itself does not have any on-board rotors. Instead, the wing is spooled out in crosswind flight, under high tension, then spooled in under very flow tension. A net amount of energy is generated each cycle at the base station.

The present work focuses on the second mechanism for energy generation, which is a practical solution when the incorporation of on-board turbines onto the wing itself presents a severe logistical burden or the wing operates in such a harsh environment that the inclusion of a rotor and generator on the wing represents too large of a cost in the event of a system failure. A single cycle of operation for these systems consists of two phases. First, the tether is spooled out under high tension, with the lifting body flying in crosswind patterns in order to generate energy. During the second phase, the lifting body is configured to minimize the tether tension and the generator is then reversed, reeling in tether and acting as a motor. This is depicted qualitatively in Fig. 2(a). Because the energy generated during the spool-out phase far exceeds the energy consumed during the spool-in phase, the net energy produced is positive.

Given the limitations of existing dynamic modeling tools, [4], [5], and [6] have investigated on-line adaptation of some attributes of the crosswind flight. Specifically, [4] and [5] seek to optimize the flight path *location* whereas this work seeks to optimize the flight path *shape*. Additionally, [6] optimizes a state setpoint trajectory, whereas this work seeks to optimize a path defined only in terms of spatial coordinates, with no reference to time. Furthermore, none of the aforementioned works considers path optimization in the context of a full spool-in, spool-out cycle.

Because the spool-out/spool-in process is highly repetitive, there is an opportunity to leverage knowledge from previous cycles in order to optimize our performance during future cycles. This repetitive nature is especially helpful in cases such as this where existing dynamic models have large associated uncertainties. In order to capitalize on this opportunity, recent work in [7] and [8] has developed a strategy for maximizing an economic performance index by altering the path geometry from iteration to iteration.

This research was supported by National Science Foundation award number 1727779, entitled "Collaborative Research: An Economic Iterative Learning Control Framework with Application to Airborne Wind Energy Harvesting", as well as award number 1538369, titled "Collaborative Research: Self-Adjusting Periodic Optimal Control with Application to Energy-Harvesting Flight".

[1]Mitchell Cobb is a PhD candidate at North Carolina State University mcobb@ncsu.edu.

[2]Kira Barton is an Associate Professor in the Department of Mechanical Engineering at the University of Michigan, Ann Arbor, MI 48109, USA bartonkl@umich.edu.

[2]Hosam Fathy is a Professor in the Department of Mechanical and Nuclear Engineering at the Pennsylvania State University, State College, PA 16802, USA hkf2@engr.psu.edu.

[4]Chris Vermillion is an Associate Professor in the Department of Mechanical and Aerospace Engineering at North Carolina State University, Raleigh, NC 27695, USA cvermil@ncsu.edu. He is also a technical advisor and equity stakeholder for Altaeros Energies, Inc.

This optimization strategy consists of two key steps which are performed at the beginning of every iteration. First, we update an estimate of the response surface, using a recursive least squares formulation. Second, we apply an iteration-to-iteration update law to adapt the path geometry, based on the estimated shape of the response surface.

The present work differs from our earlier work in [7] and [8] through (i) the application of the economic ILC strategy to a spool-out/spool-in application (where power generation is dictated by tether tension and spooling rates, rather than crosswind flight speed), and (ii) the application of this approach to a system that is tailored toward *marine hydrokinetic applications*. In particular, the contributions of this work are threefold:

1) The model initially developed in [9] and extended in [8] has been extensively modified to better reflect the dynamics of a tension-based AWE or MHK system.
2) The model parameters have been refined and sized to reflect a 100 kW system.
3) The control and optimization strategies have been adapted to AWE and MHK systems that utilize cyclic spool-out/spool-in motions to generate energy.

II. Plant Model

This work expands upon prior work by the co-authors in developing a dynamic model appropriate for a tension-based AWE or MHK system. This model, termed the "unifoil" model, utilizes the unicycle model of [9] to describe the *kinematics* of the system but derives the driving forces and moments from a physics-based model that is based on the aerodynamic characterization of the underlying lifting body. The system, characterized by two coordinate systems and a path, is shown in Fig. 3. We summarize some key features of this model, also presented in [8], here. Specifically:

1) The model is kinematically constrained to move on the surface of a sphere centered on the base station. This is the "taught-tether" assumption commonly found in the literature.
2) The system moves in the direction that it is pointing on the surface of the sphere (i.e., the familiar "no slip" condition).
3) Translational and rotational motion is driven by the aero or hydrodynamic forces and moments generated by control surfaces.

Several features have been added to the model in order to increase model fidelity, make the model applicable to hydrodynamic environments, and capture the spool-in, spool-out modes of operation. These include:

1) The inclusion of added mass effects. While these may be insignificant for a relatively heavy AWE system, they can have a profound impact on MHK systems and AWE systems that are relatively lightweight.
2) The inclusion of an actively controlled horizontal stabilizer.
3) Allowance for tether length variation.
4) Estimation of tether tension based on aero/hydrodynamic force characterizations (which is essential for characterizing power generation/consumption on a spool-out/spool-in system).
5) Sizing of system dimensions to approximate a neutrally buoyant 100 kW MHK system.

A. Translational and Rotational Dynamics

Because of the no slip condition mentioned above, the only translational acceleration of this system occurs in the direction of the bod-fixed x-axis, x_B. This results directly from the aero or hydrodynamic forces on the main wing, rudder, and horizontal stabilizer. It is calculated as

$$\begin{aligned}\ddot{x}_B =& g_x^B + \frac{\rho}{2m}\left(v_{app}^B\right)^2 \\ &\Big(A_{ref}^w C_L^w(\alpha_w)\sin(\gamma_w) - A_{ref}^w C_D^w(\alpha_w)\cos(\gamma_w) \\ &+ A_{ref}^r C_L^r(\alpha_r)\sin(\gamma_r) - A_{ref}^r C_D^r(\alpha_r)\cos(\gamma_r) \\ &+ A_{ref}^r C_L^s(\alpha_s)\sin(\gamma_s) - A_{ref}^s C_D^s(\alpha_s)\cos(\gamma_s)\Big).\end{aligned} \tag{1}$$

In this expression, $g_x B$ is the projection of the gravitational force vector onto the body fixed x-axis, m is the total mass of the system (including added mass), ρ is the fluid density, $A_{ref}^{w,r,s}$ is the reference area of the wing, ridder, or horizontal stabilizer, and $C_{D,L}^{w,r,s}$ represents the coefficients of lift and drag of the wing, rudder, and horizontal stabilizer, respectively. The aerodynamic coefficients are implemented using lookup tables.

The system induces rotational motion by generating an aerodynamic force on the rudder. This generates a moment about the body fixed z-axis, z^B, according to

$$M_z = \frac{1}{2}\rho\left(v_{app}^B\right)^2 l_f A_{ref}^r C_L^r(\alpha_r)\cos(\gamma_r), \tag{2}$$

where l_f, the length of the fuselage, determines the moment arm.

B. Added Masses and Inertias

The added mass and inertia for this system are approximated by representing the airfoil cross-sections of the aerodynamic surfaces as ellipsoids. We assume that flow comes primarily from the front of the lifting body and that rotation occurs only about the body fixed z-axis. We can then approximate the added mass from [10] as

$$m_{add} = \rho\pi\left(S_w\left(\frac{h_w}{2}\right)^2 + S_s\left(\frac{h_s}{2}\right)^2 + S_r\left(\frac{h_r}{2}\right)^2\right), \tag{3}$$

where the fluid density, ρ, along with the wing, stabilizer, and rudder spans and thicknesses, $S_{w,s,r}$, $h_{w,s,r}$ are given in table I.

In this model, the dominant added inertia effects will result from the added mass of the rudder, rotating about the body fixed z-axes, at the end of the fuselage. We approximate this added mass as a point mass at the end of

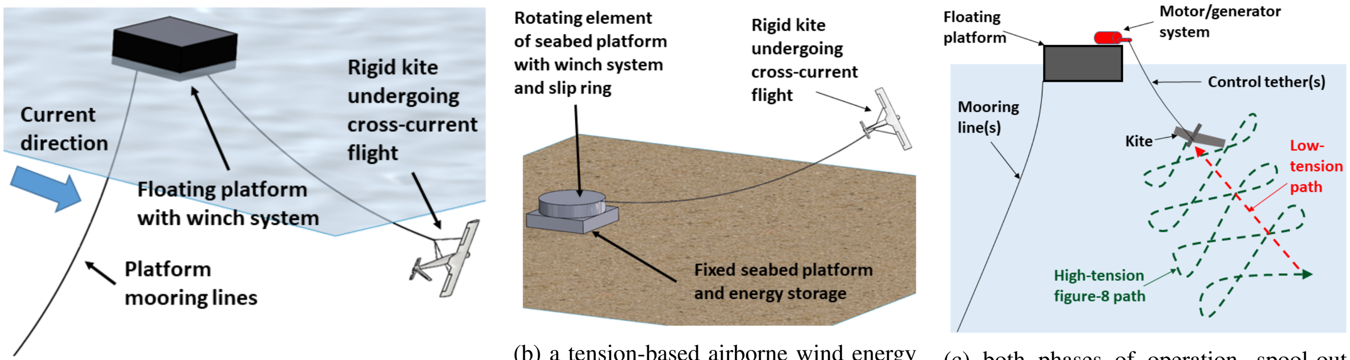
Current direction
Floating platform with winch system
Rigid kite undergoing cross-current flight
Platform mooring lines
Rotating element of seabed platform with winch system and slip ring
Rigid kite undergoing cross-current flight
Fixed seabed platform and energy storage
Floating platform
Motor/generator system
Control tether(s)
Mooring line(s)
Kite
Low-tension path
High-tension figure-8 path

(a) a tension-based marine hydrokinetic energy (MHK) system operating in crosswind flight

(b) a tension-based airborne wind energy (AWE) system operating in crosswind flight

(c) both phases of operation, spool-out (green), and spool-in (red) of a tension-based MHK system

Fig. 1: Diagram of an AWE and MHK system, along with the spool-in and spool-out phases of operation of a MHK system.

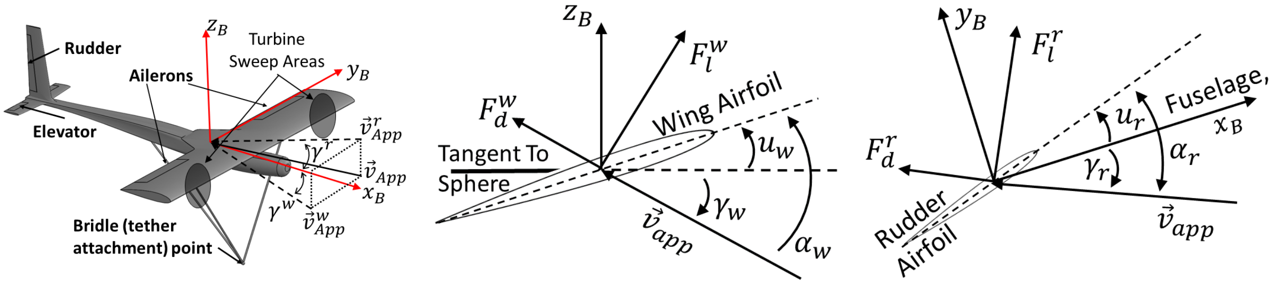

(a) an example lifting body showing the apparent wind vector, $\vec{v}^B_{App}$, along with the angles γ_r and γ_w

(b) the relationship between the commanded wing angle, u_w, γ_w, and the resulting angle of attack, α_w

(c) the relationship between the commanded rudder angle, u_r, γ_r, and the resulting angle of attack, α_r

Fig. 2: Diagrams showing the relative configuration of important aerodynamic surfaces, along with their associated controlled deflections, and angles of attack. Note that the horizontal stabilizer operates exactly like the main wing.

the fuselage. The added inertia about the body-fixed z axis is then approximated by

$$J_{add} = \rho\pi S_r l_f^2 \left(\frac{L_r}{2}\right)^2, \tag{4}$$

where l_f is the distance along the body fixed x-axis from the center of mass to the aerodynamic center of the rudder, and L_r is the reference length, or chord length of the rudder.

C. Tether Tension Estimation

The tether tension in this system is estimated by summing the components of the aero or hydrodynamic forces from the main wing and stabilizer that point in the direction of the tether. Due to the taut-tether approximation, combined with the constraint that the x_b-z_b plane is perpendicular to the sphere, this is the same as the body-fixed z-axis. As is common practice with MHK systems, the system mass has been tuned to make the system neutrally buoyant. The result is that gravity contributes nothing to the tether force. Additionally, all of the forces acting on the rudder act in the body-fixed x-y plane, so they also contribute nothing to the tether tension. The total tension is then

$$\begin{aligned} T(t) = \frac{1}{2}\rho v_{App}^2 A_{ref}^w \Big(& C_l^w(\alpha_w)\cos(\gamma_w) + C_d^w(\alpha_w)\sin(\gamma_w) \\ & C_l^s(\alpha_s)\cos(\gamma_s) + C_d^s(\alpha_s)\sin(\gamma_s)\Big), \end{aligned} \tag{5}$$

where the lift and drag coefficients of the wing and stabilizer, $C_l^{w,s}$, and $C_d^{w,s}$, are implemented as an interpolated lookup tables.

D. Parameters Tuned to Approximate 100kW MHK System

Specific parameters and dimensions of the lifting body, along with environmental conditions used in this work, are given in table I. All three aerodynamic surfaces are characterized by NACA airfoils. Initial estimates of aerodynamic parameters are obtained from XFLR5 and then corrected to account for induced drag from wind tip vortices. The main wing is modeled as an asymmetric NACA 2415 airfoil, whereas the rudder and horizontal stabilizer are modeled as symmetric NACA 0009 airfoils.

III. Control Details

To develop a control system that both optimizes and tracks the crosswind path, we divide our control strategy into two parts. The first, referred to as the lower level controller, is

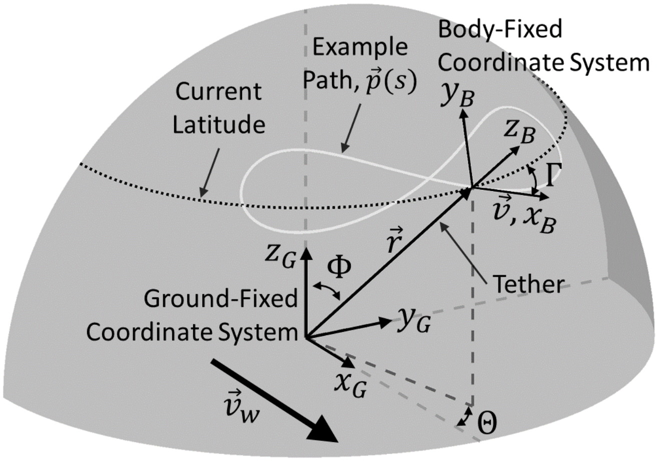

Fig. 3: Diagram showing the body-fixed coordinate system, ground fixed coordinate system, the wind direction, and an example path. Note that as the system spools in and out, the radius of the sphere, $||\vec{r}||$, will change.

Variable	Description	Value	Units
m	System mass	6184	kg
m_{add}	Added system mass	739.6	kg
J	Rotational inertia about body z-axis	104,850	kg m^2
J_{add}	Added rotational inertia about body z	724,530	kg m^2
L_w	Chord length of main wing	2	m
L_r	Chord length of rudder	0.75	m
L_s	Chord length of stabilizer	0.6	m
S_w	Span of main wing	10	m
S_r	Span of rudder	2.5	m
S_s	Span of stabilizer	2.5	m
h_w	Thickness of main wing	0.30	m
h_r	Thickness of rudder	0.0675	m
h_s	Thickness of stabilizer	0.0540	m
A_{ref}^w	Reference area of main wing	20	m^2
A_{ref}^r	Reference area of rudder	1.875	m^2
A_{ref}^s	Reference area of stabilizer	1.875	m^2
AR^w	Aspect ratio of main wing	5	-
AR^r	Aspect ratio of rudder	3	-
AR^s	Aspect ratio of stabilizer	4.167	-
l_f	Length of fuselage	8	m
V	Volume of lifting body	6.033	m^3
v_w	Fluid flow speed	1.5	m$\cdot$s^{-1}
ρ	Fluid density (seawater)	1025	kg$\cdot$m^{-3}

TABLE I: Plant parameter values sized to approximate a 100 kW marine hydrokinetic energy system.

responsible for path-following, control surface manipulation, and tether speed commands. The second, referred to as the upper level controller, is responsible for measuring and estimating performance, and then adjusting the shape of the path in order to maximize performance. The integration of both levels of the controller, along with the plant dynamics, is depicted in Fig. 4.

The lower level controller follows a conventional, closed-loop, continuous time formulation. However, the upper level controller operates on an iteration-to-iteration basis where the calculations are performed once, in between iterations, and then the updated path geometry is provided to the lower level controller. For the purposes of this work, we consider one iteration to be one complete cycle of spool-out and spool-in, in that order. This distinction between iteration-domain and time-domain control is delineated in Fig. 4.

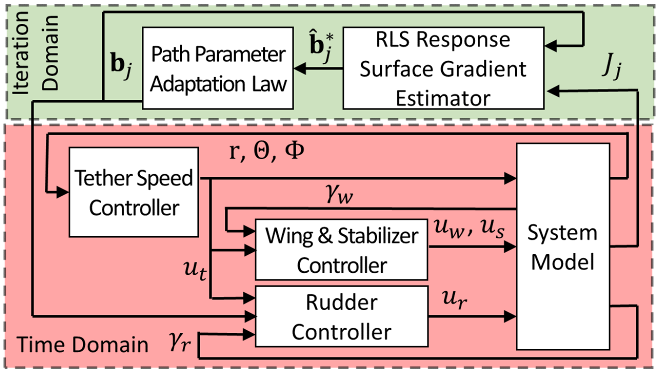

Fig. 4: A block diagram showing the iterative update strategy, applied between iterations, on top, and the lower level spool-in, spool-out, crosswind flight controller on bottom. The signals r, Θ, and Φ are the spherical radius, azimuth and zenith coordinates. The signals u_w, u_r, and u_s are the control signals for the wind, rudder and stabilizer.

A. *Lower Level Flight Control*

The lower level controller retains many of the individual components from [7] and [8] but embeds them within a switched formulation. As shown in Fig. 4, the lower level controller is comprised of individual controllers for the tether spool speed, main wing, stabilizer, and rudder.

1) Tether Speed Controller: The tether speed command, $u_r(t)$, switches between a constant spool-in speed, u_r^{in}, and a spool-out speed calculated as

$$u_r^{out}(t) = \frac{1}{3}\frac{v_{flow}(t)}{\sin\left(\Phi(t)\right)}, \tag{6}$$

where v_{flow} is the known flow speed of the surrounding liquid, and Φ is the zenith angle shown in Fig. 3. Here, $u_r^{out}(t)$ is chosen so that the horizontal component of the spool-out speed matches the optimal spool-out speed derived in [3].

Switching between spool-out and spool-in is controlled via the state machine shown in Fig. 5. The raw speed command, u_r, produced by this state machine is passed through a low pass filter in order to avoid sudden, unrealistic motion in the $\vec{r}$ direction.

2) Aero/Hydrodynamic Surface Controllers: Downstream from the tether speed controller, the controller dictating the angle of the main wing, relative to the plane tangent to the sphere, $u_w(t)$, switches between a controller designed to hold a constant angle of attack during spool-out, and a controller that attempts to reduce the tether tension resulting from the main wing to zero.

This controller estimates the tether tension resulting from the main wing by approximating the lookup tables used to calculate lift and drag coefficients in the plant, $C_l^w(\alpha)$ and $C_d^w(\alpha)$, with closed form linear and quadratic approximations. Specifically it approximates the first two terms of (5)

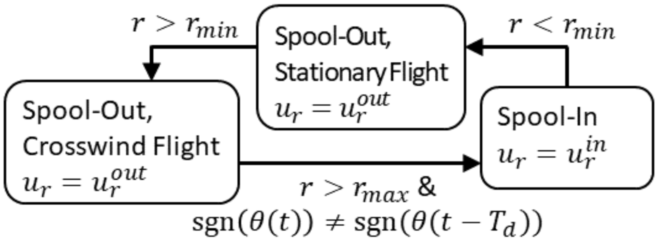
$r > r_{min}$
Spool-Out, Stationary Flight $u_r = u_r^{out}$
$r < r_{min}$
Spool-Out, Crosswind Flight $u_r = u_r^{out}$
Spool-In $u_r = u_r^{in}$
$r > r_{max}$ & $\text{sgn}(\theta(t)) \neq \text{sgn}(\theta(t - T_d))$

Fig. 5: State machine used to determine the raw tether speed, u_r. The parameters r_{min} and r_{max} are min and max tether lengths set by the user, and the third switching condition, $\text{sgn}(\theta(t)) \neq \text{sgn}(\theta(t{-}T_d))$ triggers the transition from spool-out to spool-in when the system passes back over the zero-azimuth position, or the $x_G - z_G$ plane. The time T_d is a unit time delay.

as

$$T_W = \frac{1}{2}\rho v_{App}^2 A_{ref}^w \big((k_{l0} + k_{l1}\alpha_w)\cos(\gamma_w) \\ +(k_{d0} + k_{d1}\alpha_w + k_{d2}\alpha_w^2)\sin(\gamma_w)\big), \tag{7}$$

where k_{l0}, k_{l1}, k_{d0}, k_{d1}, and k_{d2} are the coefficients of the best fit line to the linear region of the wing $C_l(\alpha)$ table and the coefficients of the quadratic fit to the wing $C_d(\alpha)$ table. The variables γ_w and γ_r are shown in Fig. 2(b) and 2(c). The value α^* that will produce no tether tension is calculated as the smallest of the two solutions to this quadratic equation at every instant in time. The commanded wing angle during reel-in is calculated from the relationship shown in 2(b), $u_w^{in} = \gamma_w - \alpha_w^*$.

The angle of attack during spool-out, u_w^{out}, is heuristically chosen to provide efficient flight, quantified by a large lift-to-drag ratio, while ensuring that the system maintains positive tether tension, quantified by a large lift coefficient. The full form of the switched wing angle controller is then

$$u_w(t) = \begin{cases} u_w^{in}(\gamma_w(t)), & u_r(t) \geq 0 \\ u_w^{out}(\gamma_w(t)), & \text{otherwise.} \end{cases} \tag{8}$$

The stabilizer controller operates in a similar fashion during spool-in, rotating about it's span to minimize drag. However, during spool-out it aligns the stabilizer to be tangent to the sphere.

The rudder controller follows the a feedback linearizing model reference control strategy discussed in [7] and [8]. For completeness, a summary is included here. Effective path following requires two components:

- First, the heading setpoint, Γ_{sp}, is calculated by picking a point a set distance ahead of the current position on the path. This is referred to as the "target" or "carrot". The heading setpoint is then calculated as the heading-on-a-sphere from the current point, to the target point,
- Second, the system heading, Γ, is controlled to asymptotically track a filtered version of the calculated setpoint, dictated by a second order reference model.

The rudder controller is implemented as a feedback linearizing model reference controller. Specifically the rudder angle controller is given as

$$u_r(t) = -\frac{J}{M_{z0}(\gamma_r)k_{L1}^r}\Big(\frac{1}{\tau^2}(\Gamma_{sp} - \Gamma) - \frac{2}{\tau}\dot{\Gamma}\Big) - \gamma_r \tag{9}$$

Here, the term $M_{z0}(\gamma_r)$ includes all the terms of equation (2) *other than* the aerodynamic coefficients C_L^r, which have been replaced with the approximated coefficient k_{L1}^r. Note that because the rudder airfoil is symmetric, k_{L0} is zero and therefore does not appear in the controller.

B. Iterative Learning-Based Path Optimization

While the lower level control strategy detailed above is designed to *track* prescribed crosswind flight paths over spool-in and spool-out cycles, it does nothing to *optimize* the crosswind flight paths themselves. In seeking to maximize the performance of the system we adapt tools from iterative learning control (ILC) to our application. This framework has been developed in prior work, specifically [7] and [8]; however, we make two significant alterations in order to extend that framework to apply to this system:

1) The performance index is adapted to fit the energy generation method of the tension-based system.
2) A single iteration has been redefined to encompass two phases of operation (spool-out and spool-in).

The performance index for this application is chosen to capture two simultaneous goals. The first term of this performance index characterizes the mean power generation over a single iteration, and the second term serves as a penalty on paths that cannot be followed accurately, helping to ensure robust and repeatable flight. Specifically, the performance index at each iteration is calculated as

$$J_i = \frac{1}{t_{e,i} - t_{s,i}} \int_{t_{s,i}}^{t_{e,i}} T(t)u_r(t) - kd_{min}(t)dt, \tag{10}$$

where $t_{s,i}$ and $t_{e,i}$ are the start and end times of the i-th iteration, $T(t)$ is the estimated tether tension, k is a scalar weight, and d_{min} is the minimum distance from the system to the path at each instant.

Using this performance index, we then apply our ILC update law to adjust the vector of parameters that define the path geometry, $\mathbf{b}$:

$$\mathbf{b}_{i+1} = \mathbf{b}_i + k_L \nabla \tilde{J}_i(\mathbf{b}) + \mathbf{E}_i \tag{11}$$

where k_L is a scalar learning gain, $\nabla \tilde{J}_i(\mathbf{b})$ is the gradient of the estimated response surface at the current iteration, and $\mathbf{E}_i$ is a persistent excitation term.

At each iteration, the estimated response surface $\tilde{J}$, is updated using a recursive least squares (RLS) estimator that assumes a quadratic dependence on each of the elements in $\mathbf{b}$. This RLS estimator includes an exponential forgetting factor that provides two benefits:

1) It helps accelerate convergence by ensuring that the response surface is weighted towards the most recently acquired data.
2) It allows the estimated response surface to adapt to reflect changing environmental conditions (such as changing wind speed).

To estimate $\hat{J}(\mathbf{b}_j)$, we model the performance index as the inner product of a regressor vector, $\mathbf{h}(\mathbf{b}) \in \mathbb{R}^q$, and a coefficient vector, $\boldsymbol{\beta} \in \mathbb{R}^q$, as $\hat{J}(\mathbf{b}_j) = \mathbf{h}(\mathbf{b_j})^T \boldsymbol{\beta}_j$. Here, $\hat{J}(\mathbf{b}_j)$ represents an approximation of the performance index, and the regressor vector structure, $\mathbf{h}(\mathbf{b}_j)$, is selected to encode the anticipated dependency of J on the basis parameters. The coefficients to the estimated response surface, $\boldsymbol{\beta}$ are then identified at each iteration, j, using recursive least squares (RLS), with an exponential forgetting factor, λ, as follows:

$$V_j = \frac{1}{\lambda}\left(V_{j-1} - \frac{V_{j-1}\mathbf{h}(\mathbf{b}_j)\mathbf{h}(\mathbf{b}_j)^T V_{j-1}}{1+\mathbf{h}(\mathbf{b}_j)^T V_{j-1}\mathbf{h}(\mathbf{b}_j)}\right), \quad \lambda \leq 1$$

$$\beta_j = \beta_{j-1} + V_j \mathbf{h}(\mathbf{b}_j)\big(J(\mathbf{b}_j) - \mathbf{h}(\mathbf{b}_j)^T \beta_{j-1}\big). \qquad (12)$$

The persistent excitation, $\mathbf{E}_i$, ensures that the measured design points contain sufficient informational richness to maintain an accurate measurement of the response surface, particularly in the presence of a changing environment.

In general, the vector of parameters that define the path, $\mathbf{b}$, can be anything, so long as they completely define a path in space. However, as is commonly the case, there is a trade off between the number of design variables and the speed of convergence. For this example, we employ a vector of two parameters:

- the overall "width" of the course, W, defined as the azimuth sweep angle spanning the course, and
- the overall "height" of the course, H, defined as the zenith sweep angle spanning the course.

Thus, the vector of iteration-varying basis parameters is $\mathbf{b}_i = [\begin{matrix} W_i & H_i \end{matrix}]^T$. The shape of the path, $\vec{p}_i(s, \mathbf{b}_i) = (r_i(s, \mathbf{b}_i), \Theta_i(s, \mathbf{b}_i), \Phi_i(s, \mathbf{b}_i))$, is then calculated from a parametric form of the figure-eight known as the Lemniscate of Gerono (see [11]), where:

$$r_i(s, \mathbf{b}_i) = r_i(t) \quad \forall j \qquad (13)$$

$$\Theta_i(s, \mathbf{b}_i) = W_i \cos\big((2s + \frac{3}{2})\pi\big), \qquad (14)$$

$$\Phi_i(s, \mathbf{b}_i) = -H_i \sin\left(2(2s + \frac{3}{2})\pi\right) + \Phi_0. \qquad (15)$$

where $s \in \mathbb{S}$ is a path variable and the manifold of all path variables, $\mathbb{S}$, is a circle with the points $s = 0$ and $s = 1$ identified as equal. The quantity Φ_0 is the mean zenith angle of the course.

IV. Results

In the following simulation results, the system was tested under a spatially and temporally constant flow profile. In this simulation, the course geometry was held constant over three full iterations, in order to allow initial transients to dissipate. The RLS estimator used to estimate the response surface was then initialized by testing five points in the design space and solving for the best fit surface. The following results represent the evolution of the system under the ILC update law but do not show the initial transient settling and initialization phases.

Variable	Description	Value	Units
τ_r	Tether speed command filter time constant	1	s
λ	Forgetting factor	0.99	-
Φ_0	Mean path elevation angle	30	deg
r_{min}	Tether speed transition point, lower	40	m
r_{max}	Tether speed transition point, upper	100	m
u_r^{in}	Tether spool-in speed	3	m s^2
α_w^{out}	Wing angle of attack during spool-out	5.7	deg
k	Performance index weight	10	kW m^{-1}
w_n	Width sensitivity normalization constant	5	deg
h_n	Height sensitivity normalization constant	0.5	deg
$\overline{w}$	Normalized width excitation amplitude	0	deg
$\overline{h}$	Normalized height excitation amplitude	0	deg
W_1	Initial course height	90	deg
H_1	Initial course width	20	deg

TABLE II: Parameters used in simulation.

A. Simulation Setup

It was observed during simulation that this system was much more sensitive to one basis parameter than the other. Accordingly, the ILC update used in simulation was performed on a set of normalized basis parameters, $\overline{\mathbf{b}}_i = [\begin{matrix} \frac{W_i}{w_n} & \frac{H_i}{h_n} \end{matrix}]^T$ where the normalization constants, w_n and h_n were chosen to reflect the relative sensitivity of the performance index, J to each basis parameter.

The persistent excitation, $\mathbf{E}_i$ was implemented as two independent unit white noise generators, indicated by the functions $W_1(i)$, and $W_2(i)$ according to:

$$\mathbf{E}_i = \begin{bmatrix} 2\overline{w}\big(W_1(i) - \frac{1}{2}\big) & 2\overline{h}\big(W_2(i) - \frac{1}{2}\big) \end{bmatrix}^T \qquad (16)$$

where $\overline{w}$ and $\overline{h}$ are normalized excitation amplitudes. Specific values of the parameters used in simulation are given in table II.

B. Simulation Results

The full three-dimensional shape of the achieved path both before and after the optimization is shown in Fig. 6. We can see that the optimization decreased the path width, W_i significantly. Although the change in the zenith basis parameter, H_i is not obvious from Fig. 6, Fig 7 shows that that it was also reduced, although to a lesser degree.

The primary components contributing to energy generation are shown in in Fig. 8. These include the rate of change of tether length, u_r or $\dot{r}$, tether tension, and the estimated power output or consumption. During spool-in (negative $\vec{r}$), the tether tension is small, and during spool-out, the tether tension is much higher, producing a large positive power output. Furthermore, it is apparent that the overall duration of the iteration was reduced between the first and last iteration. The data shown in Fig. 9 suggests that the optimization converges to an optimum. Finally, Fig. 10 shows that this optimization strategy increases the mean power output of the system by approximately 35% compared to the initial course geometry.

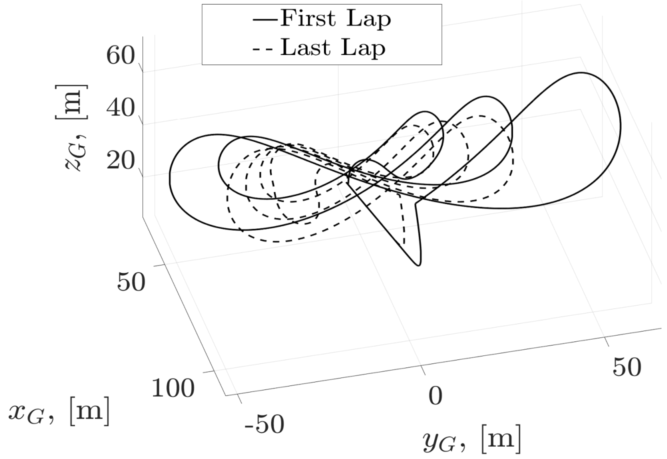

Fig. 6: Three-dimensional path of the system over a single iteration both before and after optimization.

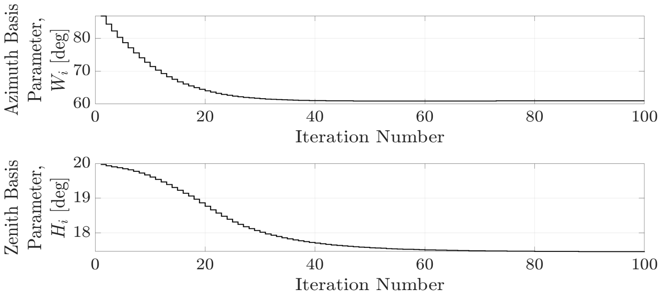

Fig. 7: Convergence of course geometry.

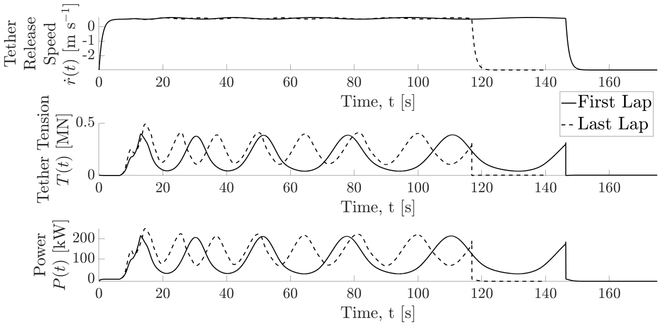

Fig. 8: Tether speed, $\dot{r}$, tether tension, T, and estimated power production over the first iteration, as well as the last iteration.

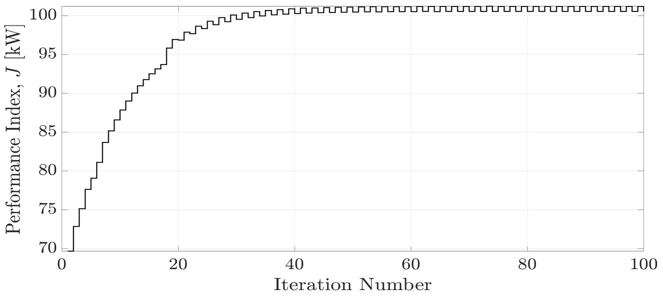

Fig. 9: Convergence of the performance index, given in (10), over the course of optimization.

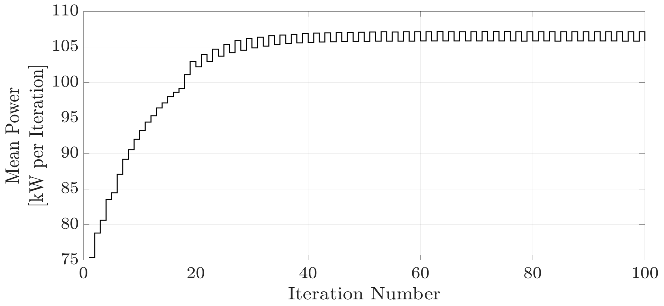

Fig. 10: Increase in mean power production, quantified by the first term in (10), over the course of optimization.

V. Conclusion

This paper presented an iterative approach for optimizing the crosswind path of a tension-based AWE or MHK system in order to maximize energy generation. By leveraging knowledge of past performance, and the parameters associated with that performance, we reduce the need for the controller to rely on complex or uncertain models. Furthermore, the optimization method is relatively computationally lightweight, thus making real-time implementation feasible. The strategy was then demonstrated on a medium fidelity model and shown to increase energy generation over the course of several iterations.

References

[1] K. Archer and K. Caldeira, “Atlas of high altitude wind power,” *Carnegie Institute for Science*, 2008.

[2] J. Bane, R. He, M. Muglia, C. Lowcher, Y. Gong, and S. Haines, “Marine hydrokinetic energy from western boundary currents,” *Annual Review of Marine Science*, 2017.

[3] M. Loyd, “Crosswind kite power,” *Journal of Energy*, vol. 4, no. 3, pp. 106–111, 1980.

[4] A. Zgraggen, L. Fagiano, and M. Morari, “On real–time optimization of airborne wind energy generators,” *Proceedings of the IEEE Conference on Decision and Control*, 2013, florence, Italy.

[5] A. Zgraggen, L. Fagiano, and M. Morari”, “Real–time optimization and adaptation of the flight of tethered wings for airborne wind energy,” *IEEE Transactions on Control Systems Technology*, vol. 23, no. 2, pp. 434–448, 2015.

[6] M. Kehs, C. Vermillion, and H. Fathy, “Online energy maximization of an airborne wind energy generator in periodic flight,” *IEEE Transactions on Control Systems Technology*, vol. PP, no. 99, pp. 1–11, 2017.

[7] M. Cobb, K. Barton, H. Fathy, and C. Vermillion, “Iterative learning–based waypoint optimization for repetitive path planning, with application to airborne wind energy systems,” *Proceedings of the IEEE Conference on Decision and Control*, 2018, melbourne, Australia.

[8] M. Cobb, K. Barton, H. Fathy, and C. Vermillion”, “Iterative learning-based path optimization for repetative path planning, with application to 3d crosswind flight of airborne wind energy systems,” *Transactions on Control System Technology*, submitted, under review.

[9] T. Wood, H. Hesse, and R. Smith, “Predictive control of autonomous kites in tow test experiments,” *IEEE Control Systems Letters*, vol. 1, pp. 110–115, 2017.

[10] K. Wendel, “Hydrodynamic masses and hydrodynamic moments of inertia,” *The Navy Department*, 1976, massachusetts Institute of Technology Translation.

[11] J. Delgado and J. M. Pena, “Progressive iterative approximation and bases with the fastest convergence rates,” *Computer Aided Geometric Design*, vol. 24, no. 1, pp. 10–18, 2007.